Plasma Actuators for flow control: suppression of the Von Karman Vortex shedding past a D-Shaped body

Mario Rapillo,[1] and Luca Pinto.[2]
Università degli studi di Napoli Federico II, Naples, Italy, 80122, Italy

This paper carries out an experimental study on the effect and limitations of DBD plasma actuators on Von Karman vortex shedding past a D-shaped body. The actuators have been placed on the trailing edge of the body and the induced flow generated by the plasma energizes the flow shortening the wake and destabilizing the coherent structures present in the baseline flow. High resolution, low-speed PIV has been utilized to characterize the boundary layer of the flow and high-speed PIV has been successively used to gather time resolved data of the wake. PSD and POD analysis show strong actuation at Reynolds number in the order of 10^5 - $U_\infty = 3.5\frac{m}{s}$ – showing the plasma actuators successfully suppressing the Von Karman shedding mode. Successive investigations on increasing velocities show gradual decrease in the actuation authority.

Abbreviations

DBD	=	Dielectric Barrier Discharge
PIV	=	Particle Image Velocimetry
PSD	=	Power Spectral Density
POD	=	Proper Orthogonal Decomposition
TKE	=	Turbulent Kinetic Energy

I. I. Introduction

VORTEX shedding is a phenomenon which occurs at all Reynolds numbers when a fluid flows past a bluff body. It is associated with pressure drops on the rear surface of the body, aeroelastic vibrations due to the oscillations of the vortex and acoustic noise. Being able to suppress the shedding is beneficial for any or all the above-mentioned problems. The origin of the vortex is linked to the inability of the flow to follow the aft part of an object, if the body is blunt enough the flow detaches from the surface creating a separation bubble: a region of back-flow. Wake instability and flow fluctuations growth will cause the bubble to burst, which will lead to a shear layer departing from the upper and lower surfaces of the body. The interaction of these shear layers is what gives birth to a vortex.

Von Karman [1] was the first to theorize the vortex shedding, addressing the stability of the phenomenon to an alternate shedding from the upper and lower surface, and quantifying the ratio of the stream-wise and transverse vortex spacing to a value of 0.28. Baily [2] provided confirmation to this theory, as well as a range of vortex strengths - Γ_1 and Γ_2 - values in which stable vortex shedding is possible: $0.38 < \frac{\Gamma_1}{\Gamma_2} < 2.62$. Once a stable vortex is formed its main characteristic is the shedding frequency. Strouhal observed that the frequency f at which vortices are shed is proportional to the flow velocity U_∞ and a geometrical parameter – the diameter d for a cylinder, the trailing edge height h for a blunt body, etc. - $f = \frac{St \cdot U_\infty}{h}$, where St is the Strouhal number and it only depends on the object shape. Blake [3] proposes a value of $St = 0.164$ for all trailing edge flows. Herr and Dobrzynski [4] found a Strouhal number equal to 0.1 for a flat plate. Jukes [5], Thomas [6] and Akilli [7] found the value of the Strouhal number for cylindrical shaped bodies to be 0.2, and 0.26 for D-Shaped bodies.

[1] Aerospace Engineering Student, DIAS, m.rapillo@studenti.unina.it .
[2] Aerospace Engineering Student, DIAS, l.pinto3@studenti.unina.it .

Control strategies can be classified in active and passive, whether an external power source is applied. Choi et al [8] provided a comprehensive study on three-dimensional control strategies. Passive actuation involves geometrical modifications to the trailing edge such as segmented trailing edges – Petrusma et al [9] – and sinusoidal trailing edges – Tombazis et al [10]. The way these methods work is by breaking the spanwise coherence of the vortices.

Active actuation implements external power supplies to energize the flow, these can be used in either an open or closed loop configuration. Examples of active actuators are an alternate distribution of blowing and suction jets – implemented by Kim et al [11] on a cylinder – synthetic jets – Paolillo, Greco, Astarita and Cardone [12] - or DBD Plasma actuators – first used in airflow control by Roth et al [13]. The reason DBD actuators are appealing is that they do not implement any mechanical moving part and provide minimal protrusion into the flow – it is safe to assume they do not alter the model's geometry. Moreover they work on electrical time scales providing very high frequency response.

II. Experimental Setup and Procedures

A. The Model

The experiments have been performed on a D-Shaped body. This model is based on a wind turbine design. It has an aerodynamic leading edge to prevent separation and ensure laminar boundary layer development, and a truncated trailing edge to shed vortices.

Physical characteristics are given in Table 1.

Table 1: Physical model characteristics

Length	Width	Thickness
450 mm	400 mm	50 mm

The coordinate system is left-handed Cartesian. Its origin is set at the middle of the model at the trailing edge. x is the streamwise direction, y is the transverse direction and z is the spanwise direction. u,v and w are the flow velocity components along the x,y and z directions, u',v' and w' are the root mean square fluctuations of the u, v and w.

B. Plasma Actuators

The plasma actuators were placed in transverse configuration – which has been proved to be the most effective [14] - on the trailing edge of the model. A single continuous actuator has been placed both on the top and bottom surface of the model.

The plasma actuator consists of:

- Covered electrode composed of one segment of copper tape laid on the trailing edge and connected to the ground.
- Dielectric layer composed of 8 layers of 0.5 mm Kapton tape on the corner of the model
- Exposed electrode composed of one segment of copper tape laid on top of the dielectric material at the end of the upper surface of the model, overlapping the covered electrode at the edge. This electrode was connected to the input terminal of the High Voltage Amplifier.

Plasma actuators parameters are given in Table 2.

Table 2: Plasma actuators parameters

Parameter	Value
Actuator input signal type	Sinusoidal
Signal peak to peak voltage	18 kV
Signal frequency	2000 Hz
Dielectric material	Kapton
Dielectric constant	4
Dielectric thickness	3 mm
Electrode Material	Copper
Electrode segments length	40 mm
Electrode segments width	5 mm

Figure 1 shows a schematic side view of the actuators.

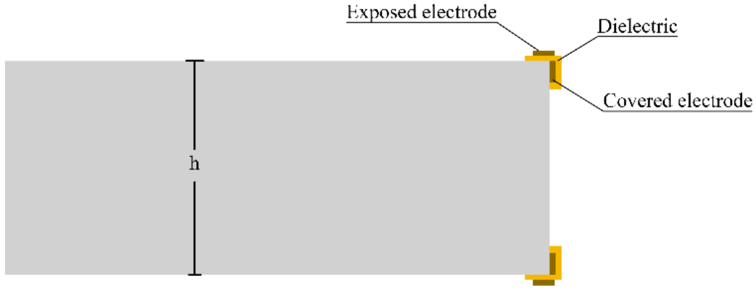

Figure 1: Schematic side view of the trailing edge showing the plasma actuators

C. PIV Setups

To acquire all the required data three different setups have been used. A low speed PIV setup to acquire the boundary layer images, and later uncorrelated images of the wake for statistical analysis, and a high-speed PIV setup to acquire time resolved data.

Given the 2-Dimensionality of the flow the imaged planes were chosen close to the middle of the span of the model, in order to minimize the end-effects due to the wind tunnel walls.

General information on the setup are given in Table 3.

Table 3: General information on the PIV setups

Seed particles	Water-glycol based
Seed particle diameter	1 μm
Imaged seed particle size	2×2 pixels
Interrogation windows	1.44 mm $\times$ 1.44 mm (check this)
Interrogation window overlap	75%

1. Low Speed PIV

The low-speed PIV setup has been used to acquire data for the boundary layer investigation and the high-resolution images of the wake for the statistical analysis. Figure 2 shows a schematic view of the wind tunnel and the model, and the two imaged planes.

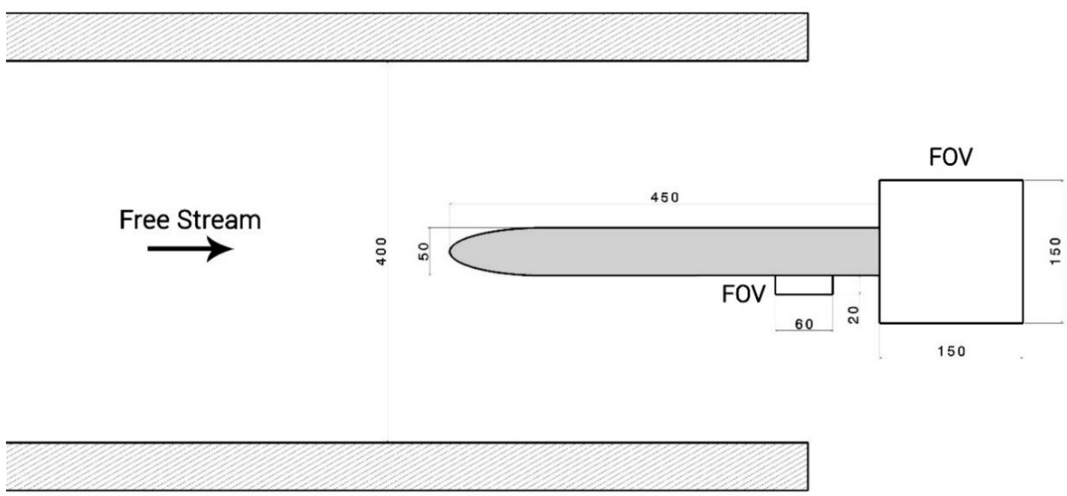

Figure 2: FOV for the Boundary Layer and wake acquisition. All dimensions in mm

To provide the necessary light for the acquisitions a Quantel Evergreen 200 laser has been used. It is a double pulsed Nd:YAG laser consisting of two cavities producing infrared light of a wavelength at 1064 nm. A second harmonic generator halves the wavelength to 532 nm – green visible light. The pulse duration had to be adjusted for each speed that has been tested, in order to keep the pixel displacement at a constant value of 10 pixels in the freestream. The laser beam diameter is less than 6.35 mm and has been made into a ~2mm sheet via a system of optics.

The camera used is a Imager Pro LX 16M. It features a complementary metal-oxide-semiconductor (CMOS) sensor; it was used with Nikkor lenses (200mm for the boundary layer acquisitions, and 105mm for the statistical analysis acquisition) and was operated in double frame mode via the controlling software (LaVision's DaVis 8.4.1).

Preliminary post-processing has been done in DaVis to reduce the noise present in every image. This was done subtracting the average minimum intensity from every image and via a multi-pass cross-correlation algorithm the velocity field is obtained.

The same setup has been used to acquire high-resolution images of the wake near the model for a statistical analysis.

Detailed information about the acquisitions can be found in table 4:

Table 4: Detailed information on the Boundary Layer acquisition setup

	Boundary Layer	**Statistical analysis**
Camera	Imager Pro LX 16M	Imager Pro LX 16M
Resolution	16 Mpx (4907 × 3697)	16 Mpx (4907 × 3697)
Pixel size	7.4 μm	7.4 μm
Lens	AF Micro-Nikkor 200mm f/4D IF-ED	Micro-Nikkor 105mm f/2.8D
Focal length f	200 mm	105 mm
Camera aperture $\boldsymbol{f}_{\#}$	8	8
Acquisition frequency	0.8 Hz	0.8 Hz
Free stream speeds tested	3-5-8-10-12-14-16-18 m/s	3-5-8-10 m/s
Laser pulse separation time dt	37-18-14-10-9-7-6 μs	37-18-14-10 μs
FOV	60 × 20 mm	150 × 150 mm
Number of images	250	500
Measurement Period	312 s	624 s

2. High Speed PIV

The high-speed PIV setup was used to acquire time resolved data.
Figure n shows the FOV of the imaged plane.

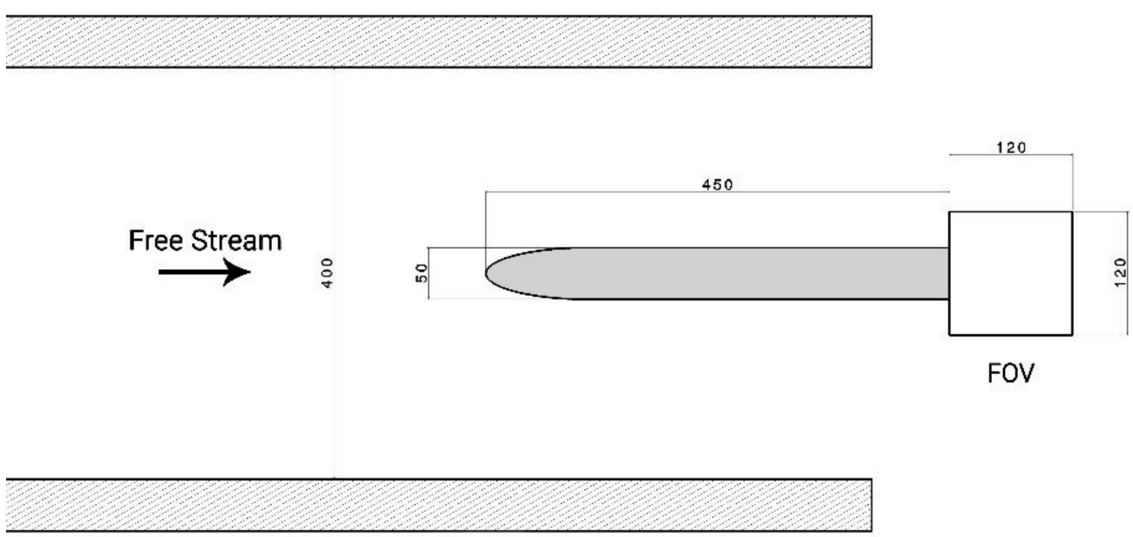

Figure 3: FOV for the Time Resolved PIV acquisition. All dimensions in mm

Detailed information about the acquisition can be found in table 5.

Table 5: Detailed information on the high-speed acquisition

Camera	LaVision HighSpeedStar 6
Resolution	1 Mpx (1024 × 1024)
Pixel size	20 μm
Lens	AF Nikkor 50mm f/1.8D
Focal length *f*	50 mm
Camera aperture $\boldsymbol{f}_{\#}$	8
Acquisition frequency	1000 Hz
Free stream speeds tested	3-5-8 m/s
Laser pulse separation time *dt*	37-18-14 μs
FOV	120 × 120 mm
Number of images	2000
Measurement Period	2 s

III. Results

A. Baseline Flow

A first investigation on the non-actuated flow has been conducted in order to characterize the boundary layer. As shown in figure 4 through an average of 500 snapshots it has been possible to reconstruct the velocity profile on the upper surface of the model. Subsequently, characteristic parameters of the boundary layer have been calculated using the equations 1-3.

$$\delta^{\star} = \int_0^{\delta_{99}} \left(1 - \frac{u(y)}{U_\infty}\right) dx \tag{1}$$

$$\theta = \int_0^{\delta_{99}} \left(1 - \frac{u(y)}{U_\infty}\right)\left(\frac{u(y)}{U_\infty}\right) dy \tag{2}$$

$$H = \frac{\delta^{\star}}{\theta} \tag{3}$$

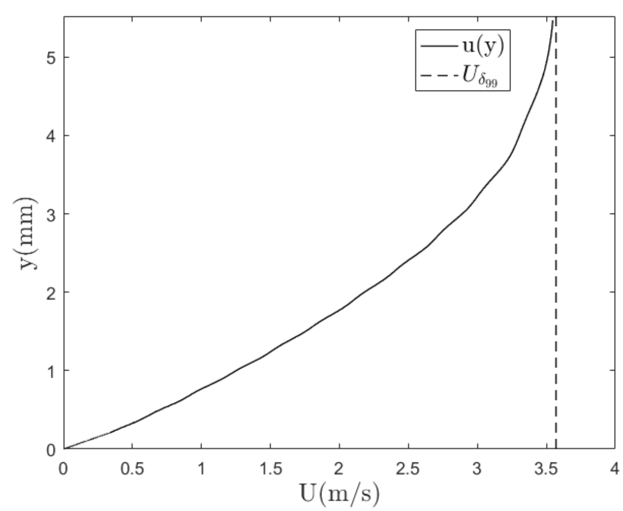

Figure 4: Boundary Layer streamwise velocity profile, $U_\infty = 3.5\ m/s$

The results have then been compared to the Blasius theory for the flat plate; figure 5 shows that experimental data for δ and $\delta^\star$ are close to the theoretical ones up to the transition free-stream velocity. For values of U_∞ higher than 16 m/s the value of δ begins to increase and to get further from the theoretical values due to the transition to turbulent flow.

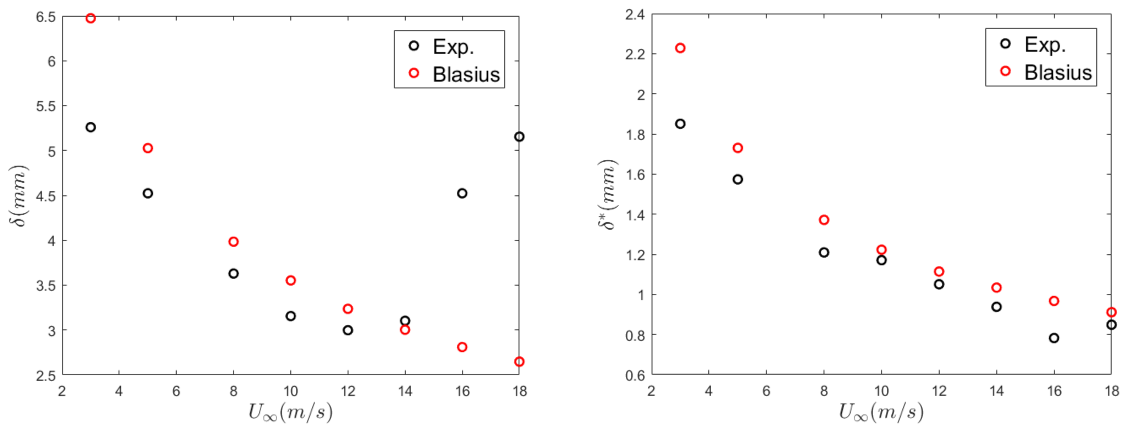

(a) (b)

Figure 5: a) Comparison between the trend of δ with the free stream velocity along the model U_∞ obtained from experimental data and the one obtained from the Blasius theory for flat plate. **b)** Comparison between the trend of $\delta^\star$ with the free stream velocity along the model U_∞ obtained from experimental data and the one obtained from the Blasius theory for flat plate

Detailed results of the investigation can be found in Table 6.

Table 6: Detailed Boundary Layer investigation results

U_∞	Re_x	$U_{\delta_{99}}$ (m/s)	$\delta_{99exp.} - \delta_{99Blas.}$ (mm)	$\delta^*_{99\,exp.}$ - $\delta^*_{99\,Blas.}$ (mm)	$\theta_{exp.} - \theta_{Blas.}$	$H_{exp.} - H_{Blas.}$
3.56	$0.9785 \cdot 10^5$	3.56	5.25 – 6.47	1.85 - 2.22	0.75 – 0.85	2.46 - 2.59
5.91	$1.6227 \cdot 10^5$	5.91	4.52 – 5.02	1.57 - 1.73	0.64 – 0.66	2.43-2.59
9.42	$2.5830 \cdot 10^5$	9.42	3.62 – 3.98	1.20 - 1.37	0.50 – 0.52	2.38-2.59
11.85	$3.2492 \cdot 10^5$	11.85	3.15 – 3.55	1.17 - 1.22	0.44 – 0.47	2.61-2.59
14.28	$3.9149 \cdot 10^5$	14.28	2.99 – 3.23	1.05 – 1.11	0.41 – 0.43	2.51-2.59
16.58	$4.5454 \cdot 10^5$	16.58	3.10 – 3.00	0.93 – 1.03	0.42 – 0.40	2.19-2.59
18.94	$5.1923 \cdot 10^5$	18.94	4.52 – 2.81	0.78 – 0.96	0.48 – 0.37	1.60-2.59
21.33	$5.8490 \cdot 10^5$	21.33	5.15 – 2.64	0.84 – 0.91	0.56 – 0.35	1.50-2.59

B. Wake analysis

In order to show the way the characteristics of the wake change when the plasma actuators are switched on it can be useful to analyze the average of the streamwise velocity carried out over 1500 snapshots, as shown in Figure 6. It can immediately be observed that the baseline flow's wake thickness is greater than the actuated one and that the reattachment point of the recirculation bubble moves downstream due to the actuators. These effects were to be expected and are due to the induced flow in the y direction generated by the plasma.

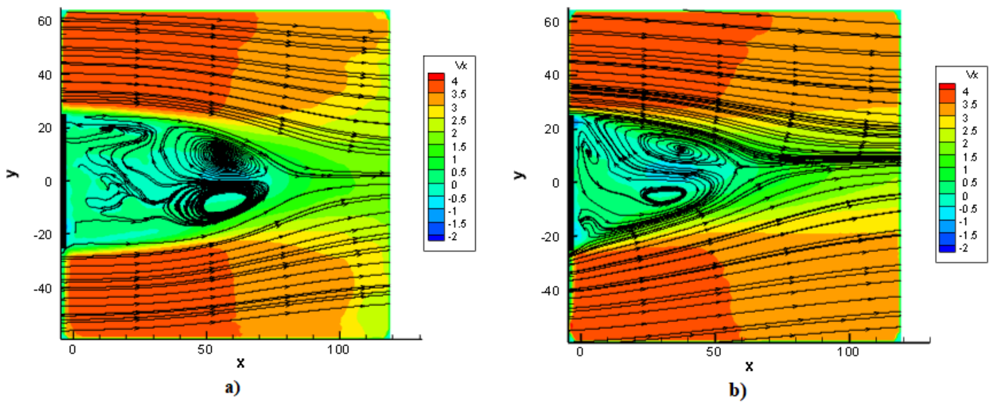

Figure 6: a) Streamwise velocity in the wake of the model averaged over 1500 snapshots for the baseline flow. **b)** Streamwise velocity in the wake of the model averaged over 1500 snapshots for the actuated flow. Both cases are referred to a free stream velocity $U_\infty = 3.5\ m/s$. The blunt base of the model is indicated in black.

C. Instantaneous vortical structures

The instantaneous x − y plane vorticity fields taken at half of the span particularly useful to observe the effect of the spanwise actuation on the baseline vortex shedding. Vorticity is calculated from the instantaneous u and v. The two time instants are separated by a non-dimensional time spacing value equal to $\Delta t^* = \Delta t \times \frac{U_\infty}{h} = 0.96$ that corresponds to half the baseline vortex shedding time period

As shown in figure 7 the coherent nature of the baseline flow appears to be severely disrupted by the actuators and the wake flow in the actuated flow is dominated by random localized vortical structures.

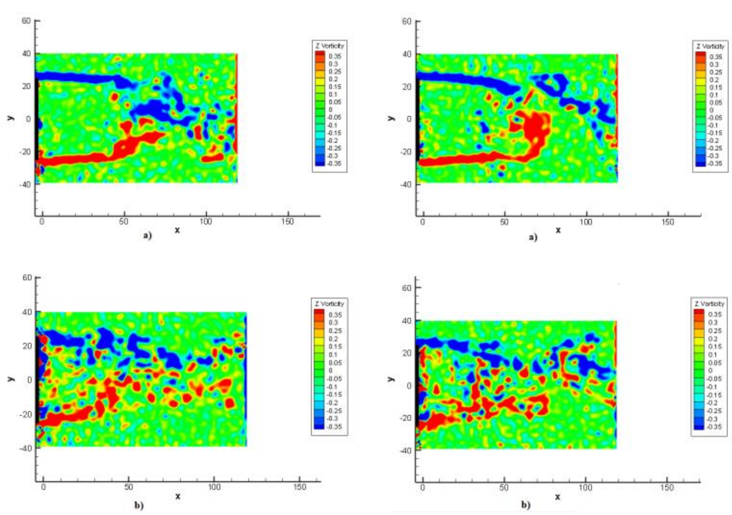

Figure 7: Instantaneous vorticity fields at two time instants half a shedding cycle apart for **a)** t = 0, **b)** t = 0.96. Both cases are referred to a free stream velocity $U_\infty = 3.5\ m/s$. The blunt base of the model is indicated in black.

D. Statistical flow fields

To further characterize the effect of the actuation an analysis on the turbulent kinetic energy production has been carried out. It is interesting to see that the dynamics of the flow in the wake change when the actuators are switched on. The Reynolds stress tensor $R_{xy} = < u'v' >$ - calculated using 1500 snapshots - shows an interaction between the Kelvin-Helmholtz instability at the corners of the trailing edge and the Karman vortex street. This can easily be seen in figure 8, in fact looking at the wake of the flow it is possible to observe that the production of kinetic energy downstream is considerably lower in the actuated flow, but it can also be observed that closer to the trailing edge the Reynolds stress tensor in the shear layer of the actuated flow is characterized by higher values with respect to the baseline flow.

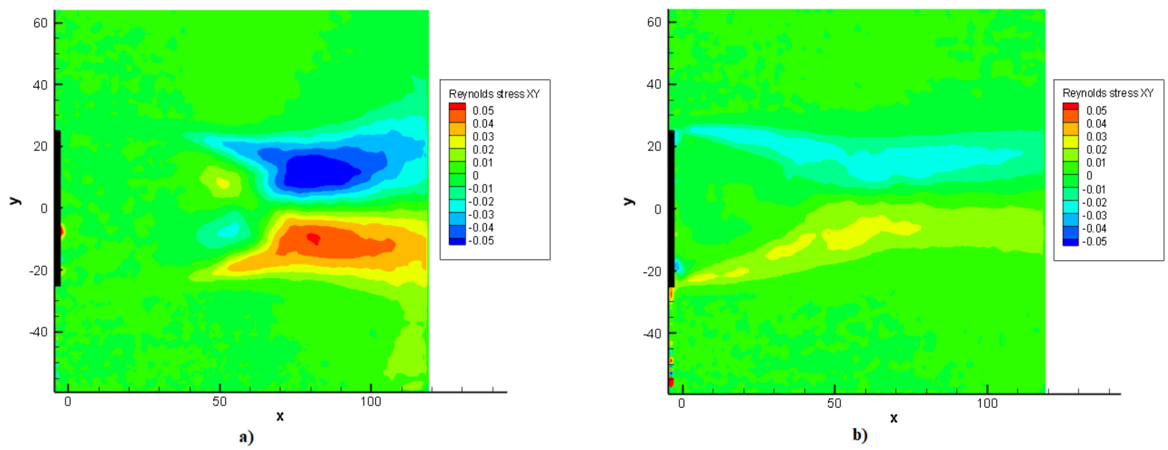

Figure 8: Reynold stress tensor R_{xy} contour for **a)** baseline flow and **b)** actuated flow. Both cases are referred to a free stream velocity $U_\infty = 3.5\ m/s$. The blunt base of the model is indicated in black.

E. Wake Power Spectrum

A PSD analysis using Welch's method has been performed in order to characterize the authority of the actuation at increasing free stream velocity U_∞. The velocity signal is probed at (x, y) = (1.2h, 0.5h), corresponding to a location in the upper shear layer and downstream of the point of separation.

The results shown in figure 9 clearly show that the effect of the actuators gets weaker as U_∞ increases. From this analysis it was also possible to evaluate the Strouhal number of the vortex shedding that - in agreement with literature - is close to 0.25.

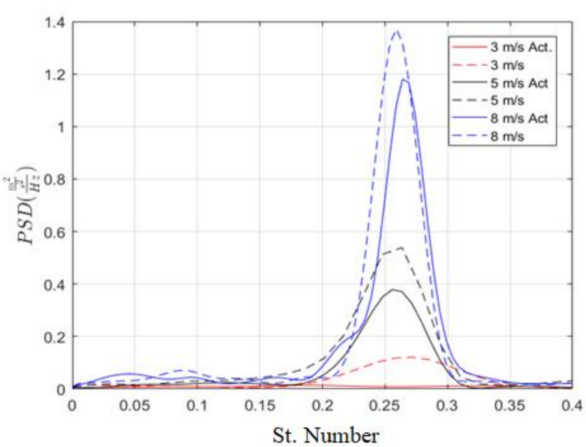

Figure 9: PSD analysis for three free stream velocity $\boldsymbol{U_\infty}$, with respect to the Strouhal number.

F. POD Analysis

Proper Orthogonal Decomposition (POD) analysis has been applied in order to evaluate the presence and the strength of periodic and coherent structures in the time-resolved x − y velocity field for both the baseline and actuated flow. Since velocity fields have been obtained via PIV over a short time period, the method of snapshots has been used. The mathematical background of this technique can be found in Chatterjee's work [15].

For each tested case 1500 images have been considered. Due to their high relative energy content, the first two POD modes are sufficient to spatially represent the Karman vortex street. The strong reduction in terms of energy percentage of the first two mode that characterizes the actuated flow is shown in figure 10.
Figures 11 and 12 show the two components of the first and second POD modes for the baseline and actuated flow. The lack of visible coherent structures in the actuated velocity field indicates a successful suppression of the modes corresponding to the Karman vortex shedding.

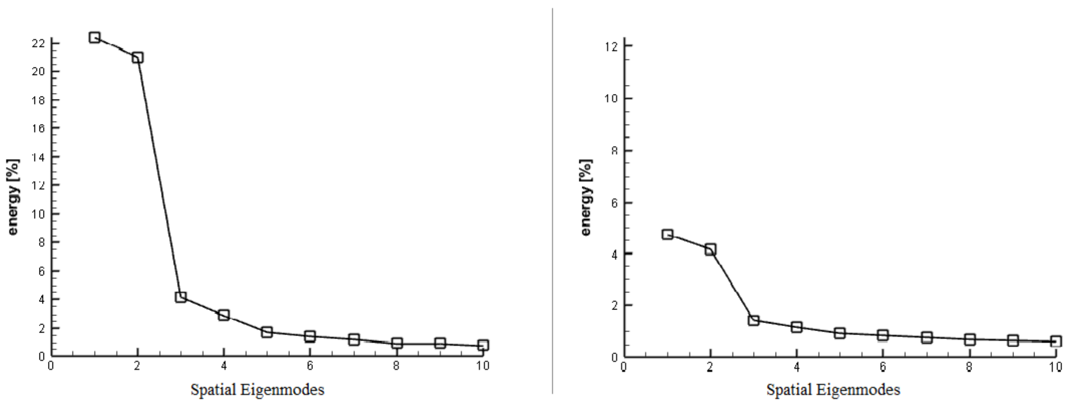

Figure 20: Individual shares of the Fluctuating KE of the wake x − y plane captured by the first ten POD modes for **a)** baseline flow and **b)** actuated flow. Both cases are referred to a free stream velocity U_∞ = 3.5 m/s.

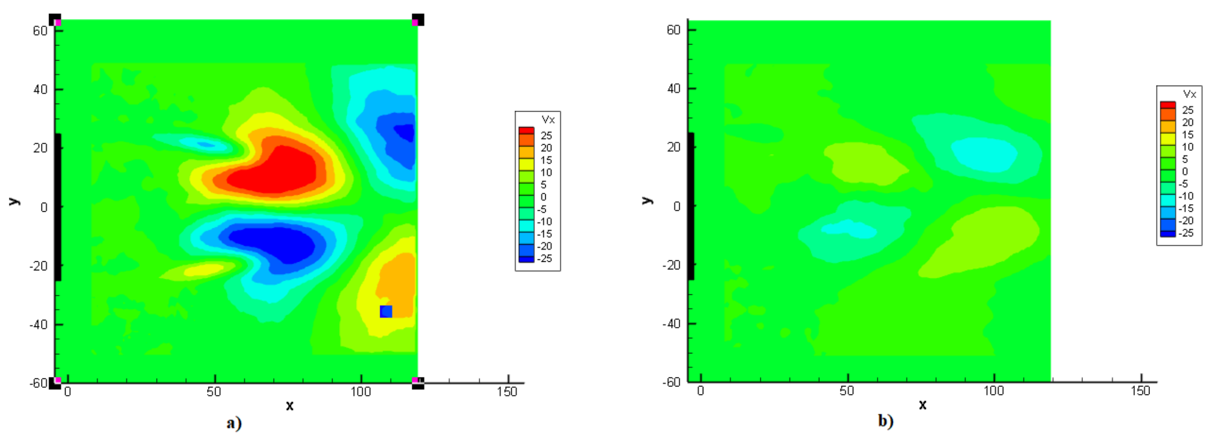

Figure 31: *u* component of the first POD mode for **a)** baseline flow and **b)** actuated flow. Both cases are referred to a free stream velocity U_∞ = 3.5 m/s. The blunt base of the model is indicated in black.

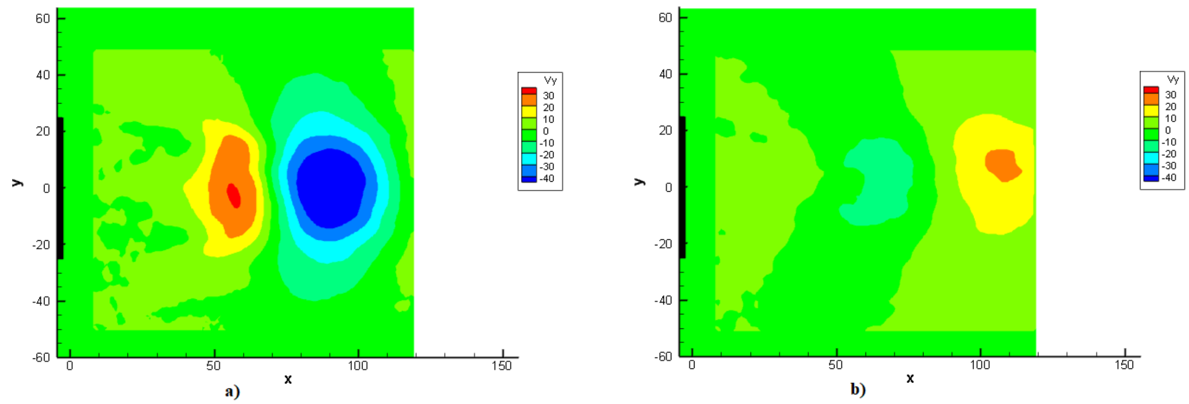

Figure 4: *v* component of the first POD mode for **a)** baseline flow and **b)** actuated flow. Both cases are referred to a free stream velocity U_∞ = 3.5 m/s. The blunt base of the model is indicated in black.

IV. Conclusion

Plasma actuators are a recent technology, being less than 20 years old. This work was intended as a further investigation on their potential as an active actuation mechanism in the Von Karman vortex suppression. Compared to previous works, the model at hand is very thick: 5 times the thickness of the previous one [13]. Keeping this in mind and knowing that plasma actuators work up to Reynolds number values in the order of $1.5 \cdot 10^5$ the flow velocities had to be kept low. The actuator used in this work was a single continuous actuator all along the trailing edge, and the investigation plane has been chosen in the middle of the model where the flow could be considered two-dimensional. Most of the experiments have been performed at $U_\infty = 3.5\frac{m}{s}$. At this velocity - corresponding to a Reynolds number $Re = 0.9785 \cdot 10^5$ – the PSD analysis shows significant reduction in the shedding frequency peaks amplitude, in agreement with the POD analysis showing the energy levels of the first two POD modes being considerably lower. Increasing the velocity of the free stream lead to a decreasing control authority of the actuators. Increasing the applied voltage of the actuators lead to an increased control authority, keeping in mind that there is a physical limitation to the applicable voltage due to the dielectric material.

For further development on this work, it would be interesting to investigate different dielectric materials that may allow to reach higher voltages and to study the energetic cost vs reward when implementing the plasma actuators. This work has confirmed their applicability, and their effectiveness, it is to be determined whether they are worth it.

V. References

[1] T.H. Karman. *Uberden Mechanismus des Widerstandes, den ein bewegter Korper in einer Flussigkeit erfart. 2. Teil.* Nachr. Ges. Wiss. Gottingen., 1912.

[2] S.C.C. Baily. *The effect of wall proximity on vortex shedding from a square cylinder.* Master's thesis, Univeristy of Western Ontario, London, NO, Canada 2001.

[3] W.K. Blake. *Mechanics of Flow-Induced Sound and Vibration,* volume vol II. Academic Press, 1986.

[4] Herr and Dobrzynski. *Experimental investigations in low-noise trailing edge design.* AIAA, 2005.

[5] T. Jukes and K.-S. Choi. *Active control of a cylinder wake using surface plasma.* IUTAM/Springer Science, 2009.

[6] F. Thomas, A. Kozlov, and T. Corke. *Plasma actuators for cylinder flow control and noise reduction.* AIAA, 2008.

[7] H. Akilli, B. Sahin, and N. Tumen. *Suppression of vortex shedding of circular cylinder in shallow water by a splitter plate.* Flow Measurement and Instrumentation, 2005.

[8] H. Choi, W.-P. Jeon, and J. Kim. *Control of flow over a bluff body.* Annual Review of Fluid Mechanics, 40:113-139, 2008.

[9] M. S. Petrusma and S. L. Gai. *Base pressure recovery for segmented trailind edge airfoils.* In 11th Australasian Fluid Mechanics Conference, University of Tasmania, Hobart, Australia, December 1992.

[10] N. Tombazis and P. W. Bearman. *A study of three dimensional aspects of vortex shedding from a blu body with a mild geometric disturbance.* Journal of Fluid Mechanics, 330:85-112, 1997.

[11] J. Kim, S. Hahn, J. Kim, D.-K. Lee, J. Choi, W.-P. Jeon, and H. Choi. *Active control of turbulent flow over a model vehicle for drag reduction.* Journal of Turbulence, 5(019), 2004.

[12] G. Paolillo, C.S. Greco, T. Astarita, G. Cardone. *Control of Von Karman vortex shedding through synthetic jet technology: momentum coefficient and non-dimensional frequency effects.* 14th International conference on fluid control, measurements and visualization, 2017.

[13] J. R. Roth, D. Sherman, and S. Wilkinson. *Boundary layer flow control with one atmosphere uniform glow discharge surface plasma.* AIAA Pap., (no. 1998-0328), 1998.

[14] G. Nati. *Suppression of vortex shedding from a truncated trailind edge by plasma actuation.* Master thesis, Delft University of Technology, 2011.

[15] A. Chatterjee. *An introduction to the Proper Orthogonal Decomposition.* Current Science, 78(7), April 2000.